



# Structural and luminescent properties of Er<sup>3+</sup> and Tb<sup>3+</sup>-doped sol–gel-based bioactive glass powders and electrospun nanofibers

Aylin M. Deliormanlı<sup>1,\*</sup>, Begüm Rahman<sup>1</sup>, Sibel Oguzlar<sup>2</sup>, and Kadriye Ertekin<sup>2,3</sup>

<sup>1</sup>Department of Metallurgical and Materials Engineering, Manisa Celal Bayar University, Yunusemre, Manisa, Turkey

<sup>2</sup>Center for Fabrication and Application of Electronic Materials, Dokuz Eylul University, Buca, Izmir, Turkey

<sup>3</sup>Department of Chemistry, Faculty of Science, Dokuz Eylul University, Buca, Izmir, Turkey

Received: 25 February 2021

Accepted: 24 May 2021

Published online:

17 June 2021

© The Author(s), under exclusive licence to Springer Science+Business Media, LLC, part of Springer Nature 2021

## ABSTRACT

In this study, sol–gel-based erbium (Er<sup>3+</sup>), terbium (Tb<sup>3+</sup>) and Er<sup>3+</sup>: Tb<sup>3+</sup> co-doped 1393 bioactive glass powders and electrospun nanofibers were prepared. Structural and morphological properties of the bioactive glasses as well as the photoluminescence characteristics were investigated in detail. The median particle size and average diameter of the prepared glass powders and fibers were in the range of ~ 1.5–3.5 μm and 280–660 nm, respectively. The steady-state photoluminescence and decay kinetics of the samples were investigated under excitation (374 nm) where only Er<sup>3+</sup> and Tb<sup>3+</sup> ions close to Si nanoclusters can be excited. All the samples prepared in the study exhibited bright green emission upon excitation at 374 nm. Results showed that the dopant concentration and the sample morphology have significant influence on the photoluminescence and decay properties of the glasses. Sol–gel-derived bioactive glass particles exhibited stronger emission intensity, whereas electrospun nanofibers showed extended decay times. In vitro bioactivity experiments revealed that Er<sup>3+</sup> and Tb<sup>3+</sup> doping did not inhibit the conversion of the glass samples to hydroxyapatite treated in simulated body fluid for 30 days. It was concluded that Er<sup>3+</sup> and Tb<sup>3+</sup>-containing 1393 bioactive glasses have a potential to be used in tissue engineering applications as well as bioimaging studies.

Handling Editor: Joshua Tong.

Address correspondence to E-mail: aylin.deliormanli@cbu.edu.tr

<https://doi.org/10.1007/s10853-021-06203-7>

## Introduction

Photoluminescent biomaterials with advanced performance have received much interest with the recent technical developments of the fluorescence labeling. The fluorescent inorganic nanomaterials such as quantum dots, latex particles and organic molecules (dyes) are used in optical imaging; however, their low biocompatibility limits the applicability of these nanoparticles for in vivo bioimaging [1]. Therefore, alternative materials such as rare earth-doped hydroxyapatite and bioactive glasses showing luminescent properties have gained attention owing to their broad applications in tissue engineering, drug release and biological imaging [2, 3].

Bioactive glasses are unique materials due to their widespread applications in tissue repair and regeneration in the form of particle, microsphere, fiber and scaffolds [4–7]. Compared to the well-known silicate-based bioactive glass composition designated as 45S5, another bioactive glass 1393 has higher SiO<sub>2</sub> concentration and some additional elements (K<sub>2</sub>O and MgO) in its composition [8]. Additionally, 1393 bioactive glasses have better processing features which permits the sintering of the glass scaffolds with lower crystallization [7, 8]. The fabrication of luminescent bioactive glasses activated with the rare earth elements has been reported previously. Fan et al. [9] studied on the drug delivery from luminescent Eu<sup>3+</sup>-doped bioactive glasses. According to their study, the drug-loaded glasses exhibited red luminescence under UV light radiation, and the emission intensities of Eu<sup>3+</sup> in the glass network changed as a function of drug release amount. This makes the drug delivery be monitored by the change of the luminescence intensity [9]. Similarly, Li et al. [10] reported the fabrication of porous photoluminescent silicate-based glass–ceramic scaffolds doped with Eu<sup>3+</sup> for tissue engineering applications. The Eu<sup>3+</sup>-doped scaffolds gained a red color radiation under UV light, and a decline in the emission intensities was examined following the cell culture experiments [10]. Saarinen et al. [11] studied on the borosilicate and the phosphate glasses in the presence of persistent luminescent SrAl<sub>2</sub>O<sub>4</sub>:Eu<sup>2+</sup>, Dy<sup>3+</sup> particles having a green luminescence up to tens of hours. It was concluded that by monitoring the changes in the luminescence, it may be possible to observe the degradation and

mineralization behavior of the bioactive glass scaffolds implanted into body [11].

Both erbium (III) and terbium (III) are rare earth elements belonging to the lanthanide group [12]. Er<sup>3+</sup> shows fluorescent properties and glow under daylight and fluorescent light [13]. It has been utilized in variety of medical applications such as laser surgery as well as the steam generation for enamel ablation in dental applications [12]. Alshemary et al. [14] studied the effects of Er<sup>3+</sup> doping on the in vitro bioactivity and the photoluminescence features of hydroxyapatite (HA). Results revealed that the synthesized materials have high bioactivity and make green and red light emissions. Similarly, Pham et al. [15] reported that Er<sup>3+</sup>-containing hydroxyapatite powders synthesized by co-precipitation method have high bioactivity and show photoluminescence properties. Mondal and co-workers [16] synthesized photoluminescent Er<sup>3+</sup>-containing hydroxyapatite nanocrystals for biomedical applications. In the study, in vitro bioactivity and optical imaging experiments performed by MG-63 cells showed the existence of nontoxic photoluminescent character. Li et al. [17] investigated the upconversion luminescence of erbium/ytterbium co-doped CaSiO<sub>3</sub> bioactive glasses. The fabricated erbium/ytterbium co-doped glasses showed green and red luminescence. The cell culture experiments indicated that the produced glasses were biocompatible and they were nontoxic to osteoblastic MC3T3-E1 cells.

Terbium oxide is a green phosphor which is utilized in wide applications such as in fluorescent lamps, biochemical sensors and X-ray intensifying screens [2, 18]. Wang et al. [19] investigated the effects of Tb<sup>3+</sup> addition on the HA forming ability and anticancer drug delivery from mesoporous bioactive glasses. Results showed that Tb<sup>3+</sup> doping at 0.5 and 1 mol% enhanced the in vitro bioactivity and doxorubicin release behavior of the bioactive glasses [19]. Qiao and co-workers [20] synthesized the Tb<sup>3+</sup>-containing HA nanoparticles by chemical deposition method. It was reported that obtained materials have enhanced photoluminescence properties and the presence of Tb<sup>3+</sup> has no detrimental effect on the microstructure of the HA. The maximum in luminescence intensity was recorded when the doping concentration of Tb<sup>3+</sup> was 8%.

Although the synthesis of Er<sup>3+</sup> and Tb<sup>3+</sup>-doped HA nanopowders and other nanomaterials has been conducted previously, few studies have been

reported on the preparation of bioactive glasses containing these elements. Additionally, in these studies, either short wavelength UV [9, 10] or upconverted luminescence of the  $\text{Er}^{3+}$ ,  $\text{Tb}^{3+}$  or  $\text{Er}^{3+}:\text{Tb}^{3+}$ -co-doped materials has been investigated [17]. However, the upconverted luminescence suffers from low emission efficiency when excited with low energy wavelengths. Therefore, the goal of the current study was to investigate the effect of  $\text{Er}^{3+}$  and  $\text{Tb}^{3+}$  doping on the structural, morphological features as well as high-energy excitation photoluminescence (@374 nm) of the silicate-based 1393 bioactive glasses prepared in the form of particles and nanofibers. The chosen excitation wavelength is both longer than the previously reported excitation energies and has the sufficient energy to excite the ions encapsulated in the glassy matrix. The decay kinetics of the particles were also investigated under excitation in nanosecond, microsecond and millisecond time regimes.

## Experimental studies

### Materials

Tetraethyl-orthosilicate (TEOS), triethyl-phosphate (TEP), calcium nitrate tetrahydrate, potassium nitrate, magnesium nitrate hexahydrate, sodium nitrate, erbium nitrate-pentahydrate, terbium nitrate-pentahydrate (all from Sigma-Aldrich, USA) were utilized as precursor materials in 1393 bioactive glass synthesis. Polyvinyl alcohol (PVA) (88.000–97.000 g/mol, 88% hydrolyzed, from Alfa Aesar) was used to prepare electrospinning solution.

### Synthesis of bioactive glass particles

$\text{Er}^{3+}$  and  $\text{Tb}^{3+}$ -containing 1393 bioactive glass powders were synthesized using sol-gel method. The chemical composition (in wt%) of the studied bioactive glasses is given in Table 1. The method followed in sol-gel synthesis has been reported previously [21]. For this purpose, a specified amount of TEOS was added into aqueous 0.3 M  $\text{HNO}_3$  solution at 25 °C and was stirred for 60 min for hydrolysis. Then other chemicals were added in sequence (depending on their reactivities) with 15-min interval, and the total solution was further stirred for 30 min. Additionally, specified amounts of  $\text{Er}(\text{NO}_3)_3 \cdot 5\text{H}_2\text{O}$  and/or

$\text{Tb}(\text{NO}_3)_3 \cdot 5\text{H}_2\text{O}$  (at 1, 3 or 5 wt%) were included into the 1393 glass solution. The final transparent solution was further stirred overnight, and then resulted glass solution was kept in a closed bottle at 25 °C without disturbing for gel formation. Gelation occurred after 5 days, and obtained gel network was aged for 48 h at 60 °C followed by drying at 120 °C for 24 h. A further heat treatment was applied at 625 °C for 4 h with a heating rate of 5 °C/min to remove the nitrates. Size reduction of the calcined powders was performed using a high-speed planetary micromill (Fritch Pulverisette 7 Premium Line, Germany) at 700 rpm for 10 min.

### Synthesis of bioactive glass nanofibers

In the study,  $\text{Er}^{3+}$  and  $\text{Tb}^{3+}$ -containing 1393 bioactive glass fibers were synthesized through electrospinning method. The technique utilized for the fabrication of the 1393 fibers was reported in detail formerly [22]. Briefly, after preparation of the bioactive glass solution as explained above an aqueous poly (vinyl alcohol) solution (10 vol%) at 1:1 ratio, 0.5 vol% surfactant (Surfynol SE, Air Products, USA) and 1 vol% ethanol was added to this solution. The resulted solution was stirred for 3 h at 25 °C for homogenization prior to electrospinning process. For the production of erbium and terbium-containing glass nanofibers, an electrospinning device (NE-300, Inovenco, TR) was used. For this purpose, the bioactive glass-PVA based solution was injected at a rate of 0.5 ml/h to a stainless steel nozzle having a diameter of 0.8 mm using a syringe pump. A stainless steel rotating cylinder was utilized as the target collector. The electrospinning experiments were performed by adjusting an 8 cm distance between the nozzle and the collector. To generate a Taylor cone at the tip of the spinneret, 20 kV voltage was applied to the electrospinning solution. The electrospun fibers were first dried at 25 °C for 48 h followed by a treatment at 250 °C for 4 h (heating rate 1 °C/min) and 625 °C for 4 h (heating rate 5 °C/min).

### Characterization

#### *Structural and morphological properties*

Phase analysis of the prepared bioactive glasses was made using an X-ray diffractometer, XRD (Philips X'Pert Pro, Netherlands), by  $\text{Cu K}\alpha$  radiation at a

**Table 1** Composition (wt%) of the bioactive glass formulations studied

Sample	SiO <sub>2</sub>	CaO	Na <sub>2</sub> O	K <sub>2</sub> O	MgO	P <sub>2</sub> O <sub>5</sub>	Er <sub>2</sub> O <sub>3</sub>	Tb <sub>2</sub> O <sub>3</sub>
1393	53	20	6	12	5	4	–	–
1Er-1393	52	20	6	12	5	4	1	–
3Er-1393	50	20	6	12	5	4	3	–
5Er-1393	48	20	6	12	5	4	5	–
1Tb-1393	52	20	6	12	5	4	–	1
3Tb-1393	50	20	6	12	5	4	–	3
5Tb-1393	48	20	6	12	5	4	–	5
1Er:Tb-1393	52	20	6	12	5	4	0.5	0.5
3Er:Tb-1393	50	20	6	12	5	4	1.5	1.5
5Er:Tb-1393	48	20	6	12	5	4	2.5	2.5

scanning rate of 0.01°/min in the range 10°s–90° 2 $\theta$ . Fourier transform infrared spectrometer (FTIR, Perkin-Elmer, Spectrum 2) was used to analyze molecular structure of the synthesized bioactive glasses. FTIR analysis was made using ATR accessory in the wavenumber range of 400–4000 cm<sup>-1</sup>. Morphology of the prepared bioactive glass powders and nanofibers was examined using a scanning electron microscope (SEM, Zeiss, Gemini 500) at an accelerating voltage of 3 keV and working distance 10 mm. Particle size of the bioactive glass powders was measured using a particle size analyzer (Malvern, Mastersizer 3000, UK), whereas the average diameter values of prepared nanofibers were obtained from the SEM images. For this purpose, at least 30 fibers were randomly selected on the images and the diameters were measured using a software.

#### Photoluminescence properties and decay analysis

Steady-state photoluminescence emission characteristics of the synthesized bioactive glass particles and nanofibers were recorded by a fluorescence spectrometer (Edinburgh instruments FLSP 920) at room temperature. Glass nanofibers were ground gently for 30 s using an agate mortar and converted into rod-like structure prior to measurements. For the lifetime measurements, time-resolved fluorescence measurement mode of the fluorescence spectrometer was utilized. The lifetime measurements in nanosecond, microsecond and millisecond regime were acquired under the excitation of pulsed laser and a microsecond flash lamp. The nanosecond regime measurements were conducted by a 367.8 nm pulsed laser, and the pulse width was much shorter (118.2 ps) than the average decay times of the glass samples. The emission data were acquired at the

maximum emission wavelength of each type of sample. A microsecond flash lamp was utilized during the measurements performed in the microsecond and millisecond regime. The IRF was recorded using a colloidal silica-water suspension (LUDOX 30%, Sigma-Aldrich).

#### *In vitro* bioactivity

Hydroxyapatite forming ability of the prepared bioactive glasses in the form of particle and nanofiber was examined in simulated body fluid (SBF) at 37 °C under static conditions. SBF was prepared based on the protocol reported by Kokubo et al. [23] Bioactive glass samples were immersed in SBF (1 gr sample per 500 ml SBF) having an initial pH of 7.4 and kept in SBF for 30 days in an incubator. After 30 days, samples were extracted from SBF and dried at 60 °C at least for 48 h prior to characterizations. Hydroxyapatite conversion of the SBF-treated samples was examined using SEM.

## Results and discussion

### Bioactive glass particles

SEM micrographs showing particle morphology of the bare and Er<sup>3+</sup> and/or Tb<sup>3+</sup>-doped 1393 bioactive glass powders synthesized by the sol-gel technique is given in Fig. 1. The prepared powders containing irregular shape particles were in the size range of 1.45–3.57  $\mu$ m based on the particle size analyzer measurements (Table 2). However, SEM micrographs demonstrate the presence of much finer particles having a diameter of  $\sim$  50 nm. The average particle sizes of the Er<sup>3+</sup> and Tb<sup>3+</sup>-doped 1393 bioactive glass

**Figure 1** SEM micrographs of the bioactive glass powders synthesized (calcined at 625 °C) in the study **a** 1393, **b** 5Er-1393, **c** 5Tb-1393, **d** 5Er:Tb-1393.

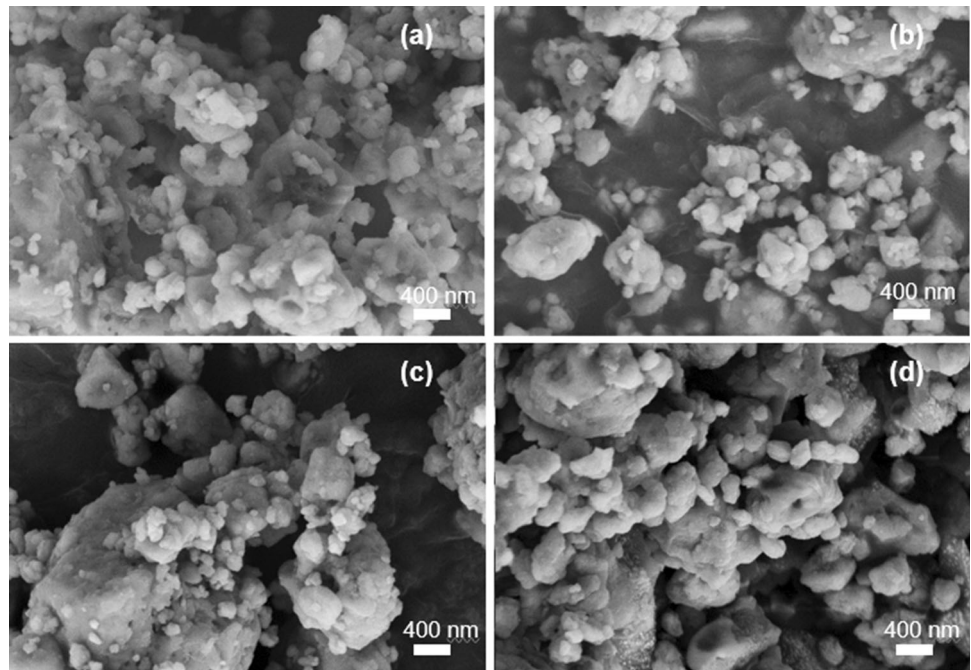


**Table 2** Particle size of the of the sol–gel-derived bioactive glass powders synthesized in the study

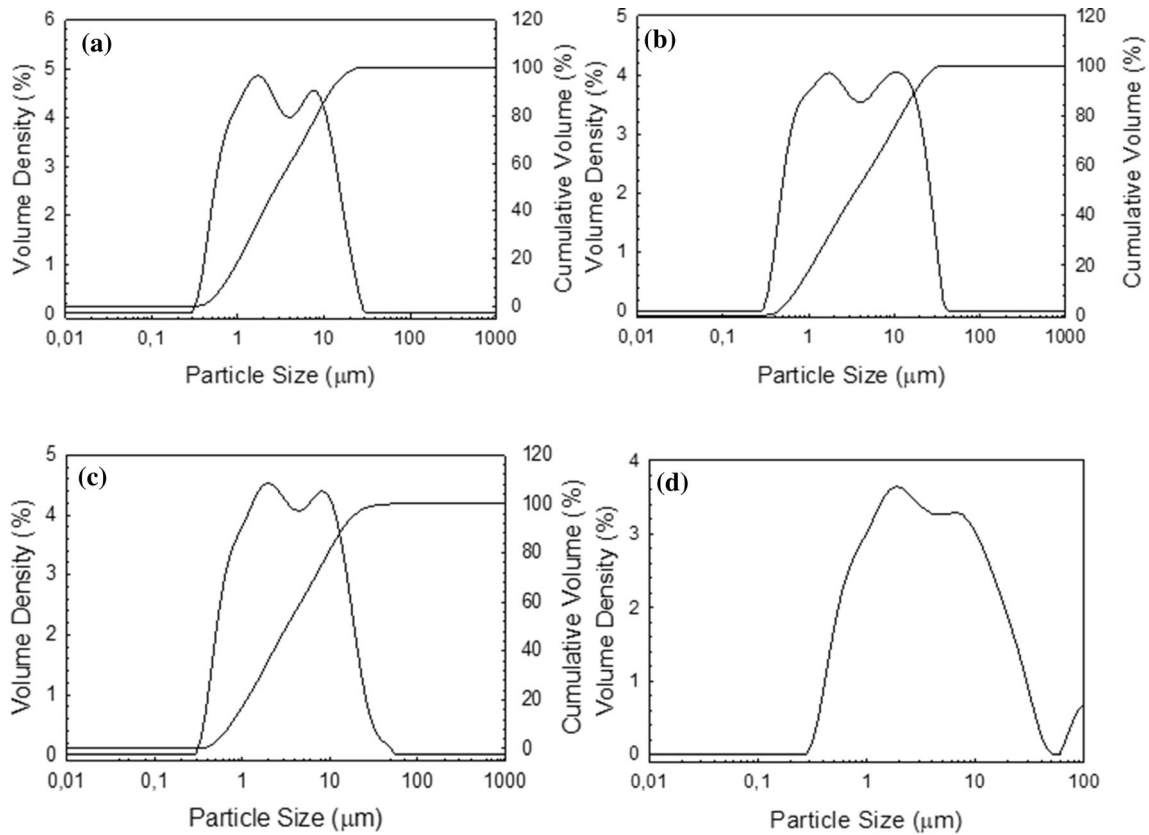
	$d_{10}(\mu\text{m})$	$d_{50}(\mu\text{m})$	$d_{90}(\mu\text{m})$
1393	0.713	2.79	11.9
1Er-1393	0.707	3.21	14.1
3Er-1393	0.741	3.57	17.0
5Er-1393	0.714	3.59	17.8
1Tb-1393	0.718	3.22	12.6
3Tb-1393	0.669	2.51	11.0
5Tb-1393	0.742	3.22	14.11
1Er:Tb-1393	0.628	1.96	7.31
3Er:Tb-1393	0.555	1.46	3.59
5Er:Tb-1393	0.544	1.45	3.32

particles were in close proximity, and the type of the dopant did not significantly affect particle size. Er<sup>3+</sup> and Tb<sup>3+</sup>-activated bioactive glass particles exhibited bimodal size distribution (Fig. 2).

XRD analyses shown in Fig. 3 revealed that all of the bioactive glass powders calcined at 625 °C for 4 h in air atmosphere were mainly amorphous at all doping concentrations. Few low-intensity peaks detected in some samples may be attributed to the existence of NaNO<sub>3</sub> and KNO<sub>3</sub> phases in the structure (Fig. 3b). Previously, similar types of crystalline peaks were also observed in XRD pattern of sol–gel-derived 1393 bioactive glass powders heat treated at

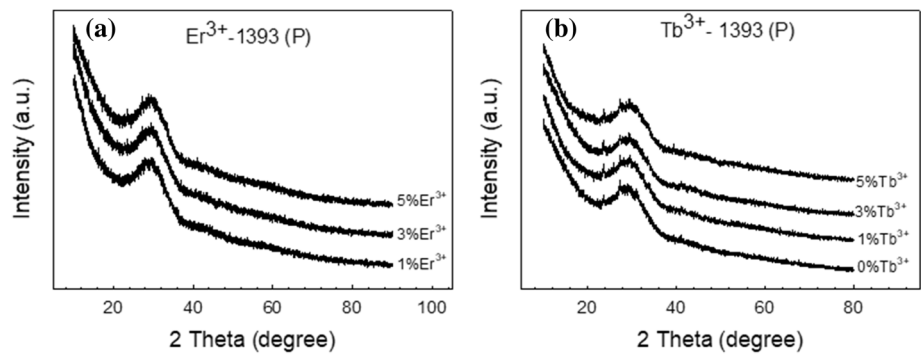
610 °C. These peaks were eliminated through a calcination performed at 625 °C. Therefore, existence of few nitrate peaks in Fig. 3b may be attributed to the conditions in furnace atmosphere [21]. However, in general results showed that calcination at 625 °C was sufficient to remove most of the nitrates from the structure resulting from the precursor materials and avoid formation of crystalline phases such as combeite observed at higher temperatures.

Figure 4 depicts the FTIR spectra of the bare, as well as the erbium and terbium-containing bioactive glass particles. It is known that there are 4 main regions (around 480, 750, 940 and 1100 cm<sup>-1</sup>) in the IR spectra of the silicate-based glasses [24]. Accordingly, the peak observed in the spectra at 932 cm<sup>-1</sup> was due to the Si–O stretching mode of non-bridging oxygen's and the peak obtained at right-hand side of this band at 1010 cm<sup>-1</sup> can be assigned to Si–O–Si asymmetric stretching of bridging oxygen's [24, 25]. Metal alkoxides of Si(IV) demonstrate absorption bands assigned to  $\nu(\text{M–O})$  stretching modes around 800 cm<sup>-1</sup> [26]. The IR peaks at 759 cm<sup>-1</sup> are assigned to  $\nu_s(\text{Si–O–Si})$  bending vibration. The peak observed at 445 cm<sup>-1</sup> is attributed to the O–Si–O bending vibration mode [24, 27]. A shift in peak positions was not obtained in the spectra of bioactive glass samples as a function of dopant concentration.

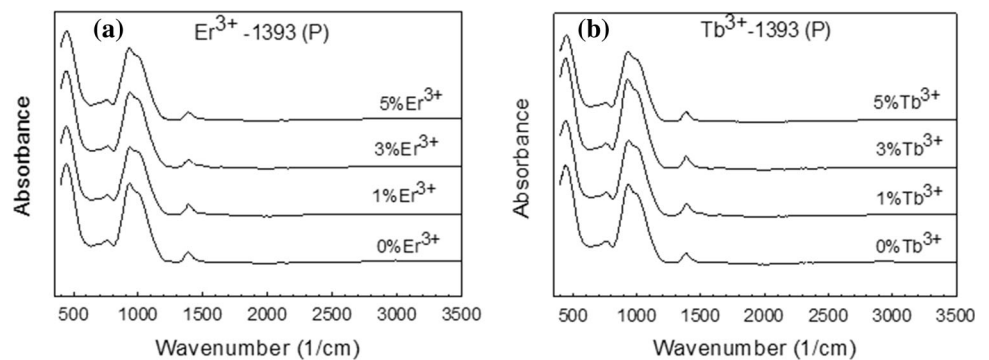


**Figure 2** Graphs showing the particle size distribution of the sol-gel-derived glass particles **a** 1393, **b** 5Er-1393, **c** 5Tb-1393, **d** 5Er:1393.

**Figure 3** XRD diagrams of the sol-gel-derived glass particles containing **a** erbium and **b** terbium.



**Figure 4** FTIR spectra of the sol-gel-derived glass particles containing **a** erbium and **b** terbium.



### Bioactive glass nanofibers

SEM micrographs showing the morphology of the electrospun bioactive glass nanofibers synthesized in the study are given in Fig. 5. Results showed that it was possible to obtain bead free, continuous 1393 bioactive glass fibers in the absence and presence of  $\text{Er}^{3+}$  and  $\text{Tb}^{3+}$  ions using electrospinning technique. The surface of the nanofibers was smooth, and any grain formation was not observed on the surface of the glass nanofibers calcined at 625 °C. Based on the SEM micrographs, the average fiber diameter of the

bare 1393 glass was measured to be  $467.9 \pm 92$  nm. On the other hand, average fiber diameter of the 5%Er and 5%Tb-containing bioactive glass samples was  $665.5 \pm 185$  nm and  $283.2 \pm 109$  nm, respectively. Similarly, fiber diameter of the bioactive glass sample containing 5%Er:Tb was measured to be  $505.3 \pm 151$  nm. Fiber diameter distribution of the bioactive glass samples containing  $\text{Er}^{3+}$  and  $\text{Tb}^{3+}$  at highest concentration is given in Fig. 6. Similar results were obtained for the samples consisting related rare earth elements at other doping concentrations.

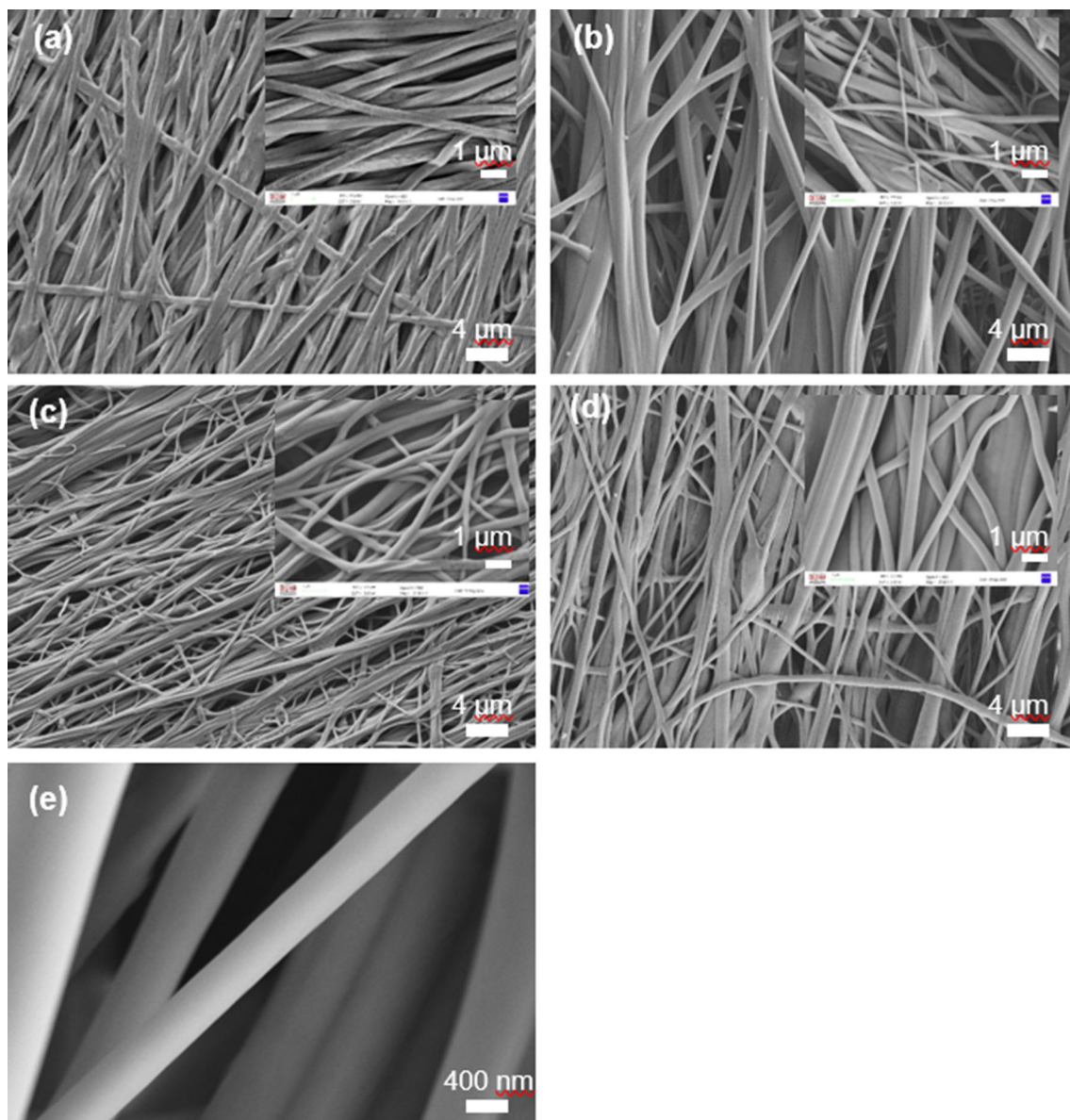


**Figure 5** SEM micrographs of the electrospun bioactive glass nanofibers synthesized (calcined at 625 °C) in the study **a** 1393, **b** 5Er-1393, **c** 5Tb-1393, **d**, **e** 5Er:Tb-1393.

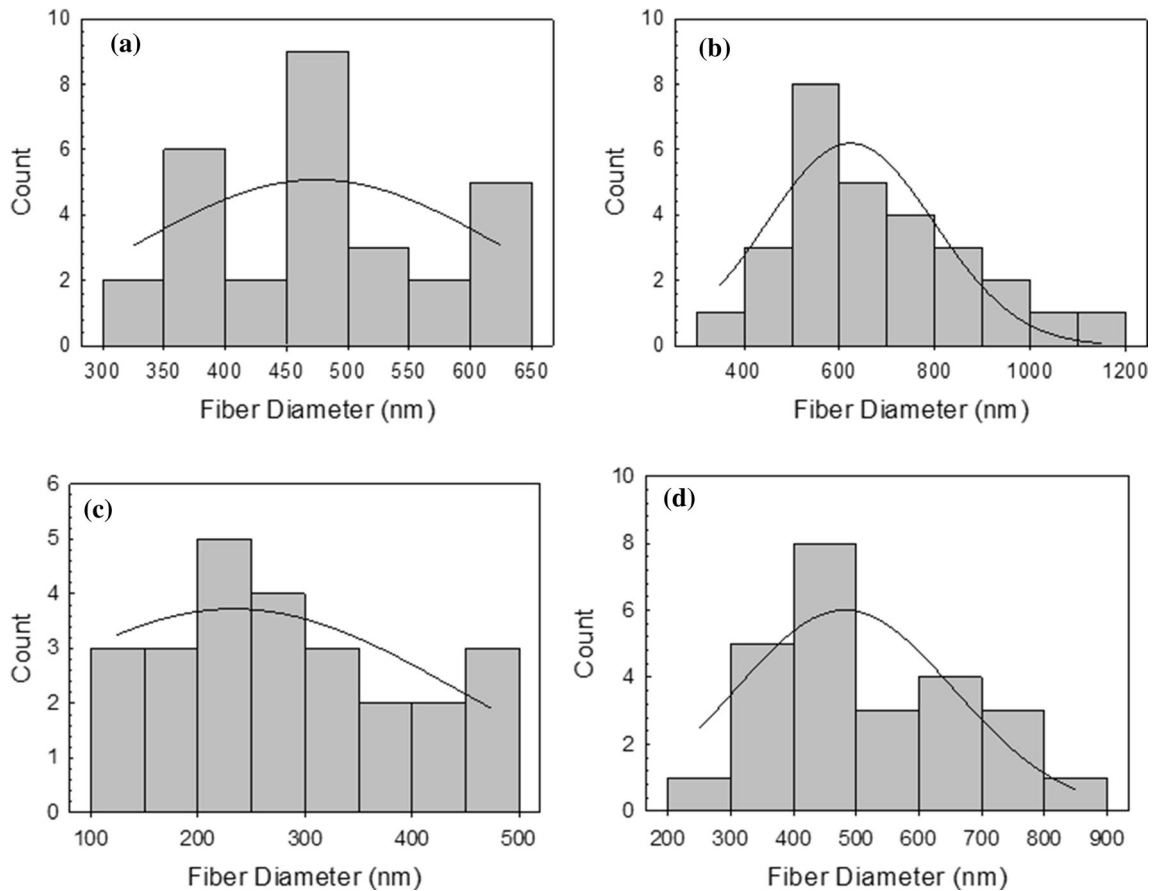


**Figure 6** Graphs showing the fiber diameter distribution of the electrospun glass nanofibers prepared in the study **a** 1393, **b** 5Er-1393, **c** 5Tb-1393, **d** 5Er:Tb-1393.

XRD analysis results of the bioactive glass nanofibers synthesized in the study are shown in Fig. 7. Accordingly, all of the  $\text{Er}^{3+}$  and  $\text{Tb}^{3+}$ -containing samples in the form of nanofibers kept their amorphous structure after calcination at  $625\text{ }^\circ\text{C}$  and all of the nitrates were removed from the structure during calcination process.

FTIR spectra of the nanofiber-based samples shown in Fig. 8 demonstrates a similar molecular

structure with the sol-gel-derived bioactive glass particles. However, for the  $\text{Er}^{3+}$ -containing 1393 bioactive glass fibers a shift in peak position at  $1006\text{ cm}^{-1}$  was recorded to lower wavelengths representing Si–O–Si asymmetric stretching. For the 3%Er and 5%Er-containing samples Si–O stretching vibrations were obtained at  $932\text{ cm}^{-1}$ . Similarly, a shift was observed for the peak assigned to Si–O stretching to lower wavelengths for 3% and

**Figure 7** XRD diagrams of the electrospun glass nanofibers containing **a** erbium and **b** terbium.

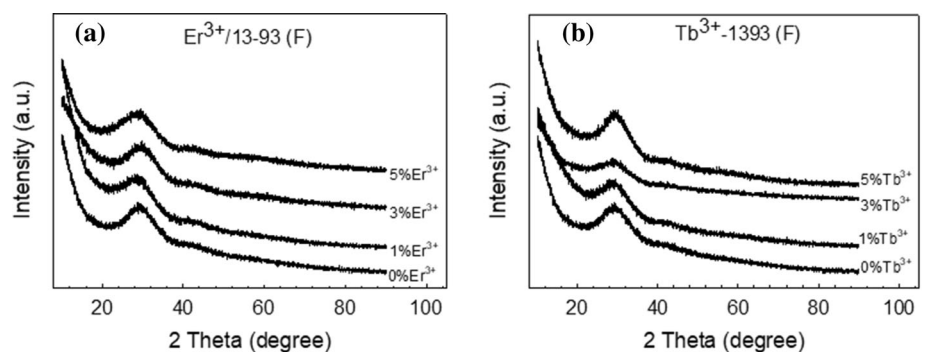
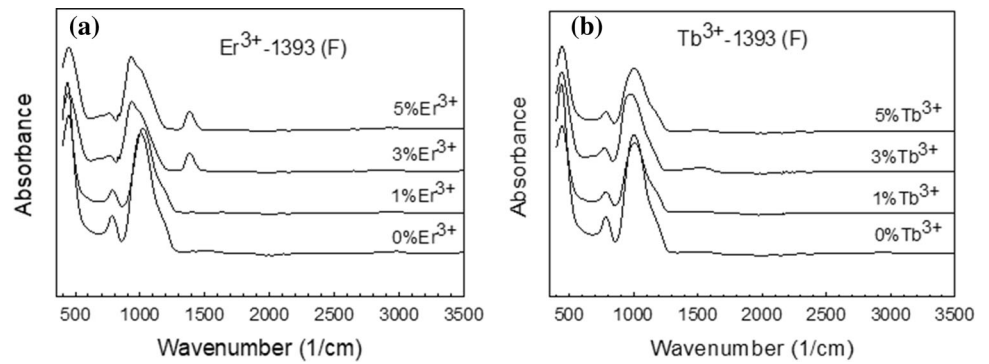




**Figure 8** FTIR spectra of the electrospun glass nanofibers containing **a** erbium and **b** terbium.



5%Er-doped glass fibers. In case of Tb<sup>3+</sup>-containing glass fibers again, a slight shift was seen for the Si–O–Si stretching peak to lower wavelengths starting from 1%Tb to 995 cm<sup>-1</sup>. The wide absorption band at about 450 cm<sup>-1</sup> that is assigned to O–Si–O bending vibration was independent of glass composition [27]. If a network modifier is included into an amorphous SiO<sub>2</sub> structure, some of the Si–O bonds are broken and the negative charge of the oxygen ion is then compensated by the modifier ion [28]. In the current study, Er<sup>3+</sup> and Tb<sup>3+</sup> presumably acted as a modifier ion in the silica glass network during nanofiber synthesis.

**Steady-state photoluminescence properties**

In the study, photoluminescence (PL) spectra of the Er<sup>3+</sup> and Tb<sup>3+</sup> -containing sol–gel-based 1393 bioactive glass particles and electrospun nanofibers were recorded. Effect of activator element and concentration as well as the glass morphology on the PL properties was investigated. Figure 9a, b shows the

excitation and emission spectra of the bare and the Er<sup>3+</sup>-doped 1393 bioactive glasses in the form of particles and fibers, respectively. Upon excitation at 374 nm, the dopant-free 1393 glass particles yielded emission bands centered at 506 and 566 nm arising from the optical transitions from the ns<sup>2</sup>-levels (n = 1,2,3,...), related to structural units of the glass matrix.

Previous studies on the optical property of silica glass demonstrated that there are many optic-active defect centers with strong absorption in the UV range [29]. Additionally, the defect designation in multi-component structures is complex. The oxygen-related defects are oxygen hole centers, where a hole is trapped in a nonbonding p-orbital of an oxygen. Silicon-related defect centers could be trapped holes on one or two non-bridging oxygens on the same SiO<sub>4</sub> tetrahedron [30].

The sol–gel-derived Er<sup>3+</sup>-doped 1393 glass powders appeared pink under sunlight and the color intensity increased with the increment in Er<sup>3+</sup> concentration. Under 374 nm light irradiation, Er<sup>3+</sup>-containing glass

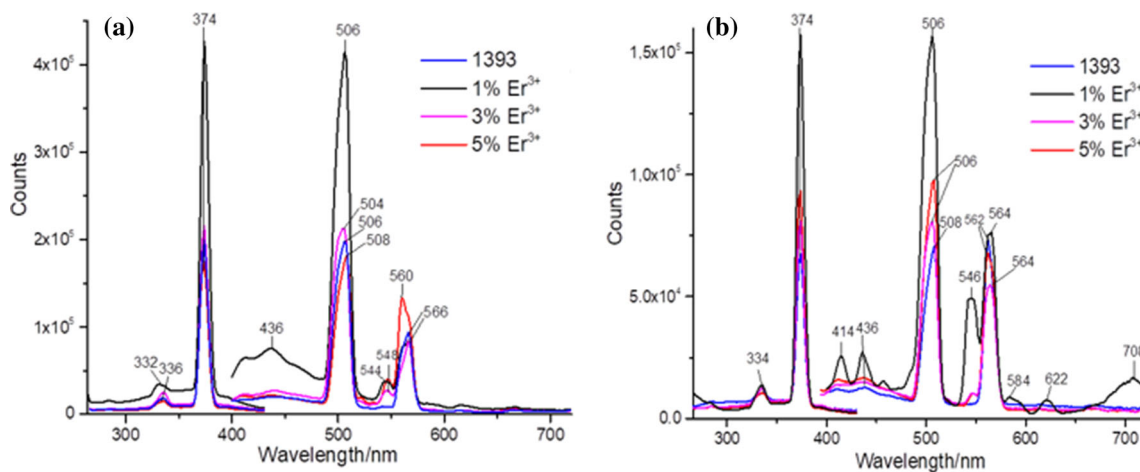


**Figure 9** Excitation and emission spectra of the Er<sup>3+</sup>-containing bioactive glass **a** particles, **b** nanofibers.

particles exhibited emission bands corresponding to blue (436 nm) and green (506, 546 and 566 nm) wavelengths. The observed emission of the  $\text{Er}^{3+}$ -doped glasses at green emission band at 566 was assigned to  ${}^4\text{S}_{3/2} \rightarrow {}^4\text{I}_{15/2}$  transitions from the excited states to the ground state of the  $\text{Er}^{3+}$  [14, 16]. On the other hand, the emission associated with blue band was attributed to  ${}^4\text{F}_{7/2} \rightarrow {}^4\text{I}_{15/2}$  transition [16].

The  $\text{Er}^{3+}$ -containing electrospun 1393 nanofibers exhibited the similar bands centered at 506, 546 and 564 nm, upon excitation at 374 nm. Additionally, 1%Er-doped glass nanofibers yielded some further weak intensity bands at 414 nm and 708 nm corresponding purple and red emission. The purple band was assigned to  ${}^4\text{F}_{3/2} \rightarrow {}^4\text{I}_{15/2}$  transition [16], and the red band in the PL spectra observed at 708 nm was assigned to the n–L shell electronic transition [14]. A decline in peak intensities was observed as the  $\text{Er}^{3+}$  ion concentration was ascended for both type of glass samples which may be attributed to the concentration quenching beyond the doping level of 1 wt% due to a non-radiative decay process. This behavior may be due to an enriched coupling to quenching sites (such as small quantities of OH sites) as a result of excitation migration at high  $\text{Er}^{3+}$  concentration [31]. Previously, quenching in the green luminescence was reported to be based on the cross-relaxation process between the two neighboring  $\text{Er}^{3+}$  ions [32, 33]. Upon doping with  $\text{Er}^{3+}$ , the rare earth ions substitute the alkaline earths in the structure and are more strongly coordinated by the  $\text{O}^{2-}$ . A potential charge mismatch between the  $\text{Ca}^{2+}$  and/or  $\text{Mg}^{2+}$  and  $\text{Er}^{3+}$  may be resulted in enhanced photoluminescence intensity even at 1% dopant concentration, due to the hypersensitivity of these electric dipole transitions of  ${}^5\text{D}_0 \rightarrow {}^7\text{F}_2$ . However,  $\text{Tb}^{3+}$  cross-relaxation processes ( ${}^5\text{D}_3 \rightarrow {}^5\text{D}_4 \leftrightarrow {}^7\text{F}_6 \rightarrow {}^7\text{F}_0$ ) strongly favored by higher doping concentrations [34]. On the other hand, the co-existence of  $\text{Eu}^{3+}$  and  $\text{Tb}^{3+}$  can provide extra channels to depopulate the erbium's emission levels by energy transfer mechanisms. Owing to this fact, the radiative spontaneous emission of co-doped samples can be different from the  $\text{Er}^{3+}$ -doped glasses [34]. Results of the current study also revealed that emission intensities of the sol–gel-derived glass particles were stronger compared to the electrospun glass nanofibers.

The mechanism observed in luminescence of  $\text{Er}^{3+}$ -doped hydroxyapatite was discussed previously by Alshemary et al. [14] Accordingly, low

energy electrons of  $\text{Er}^{3+}$  present in  ${}^4\text{I}_{15/2}$  are excited to  ${}^4\text{G}_{11/2}$  state followed by non-radiative decay and this leads to populate  ${}^4\text{G}_{11/2}$ ,  ${}^4\text{F}_{5/2}$ ,  ${}^4\text{F}_{7/2}$  and  ${}^2\text{H}_{11/2}$  excited states. The radiative decay from  ${}^2\text{H}_{11/2}$  and  ${}^4\text{S}_{3/2}$  to  ${}^4\text{I}_{15/2}$  enhances green emission [14, 32, 33].

It is also important to note that direct excitation of the  $\text{Er}^{3+}$ -doped samples can be achieved around 980 nm which concur with the energy level of second excited state of the  $\text{Er}^{3+}$  ion, and incident photons may directly be absorbed by these ions. Therefore, in most of the previously published studies, upconverted red and green luminescence of the  $\text{Er}^{3+}$ -doped materials have been studied [17, 35]. On the other hand, when  $\text{Tb}^{3+}$  was co-doped with  $\text{Er}^{3+}$ , energy transfer from the  ${}^4\text{I}_{11/2}$ ,  ${}^4\text{I}_{13/2}$  states of the  $\text{Er}^{3+}$  ion to the  ${}^7\text{F}_0$  levels of  $\text{Tb}^{3+}$  is possible. However, despite the numerous efforts made by researchers, such kind of upconverting materials are still suffering from low emission quantum efficiency. Herein we performed excitation by using 374 nm where incident photons are non-resonant with the  $\text{Er}^{3+}$  energy levels, directly. The potential excitation path therefore is due to the absorption of the energy by Si nanoclusters and subsequent energy transfer to the erbium ions [35].

The excitation and emission spectra of the bare and the  $\text{Tb}^{3+}$ -containing 1393 bioactive glasses in the form of particles and fibers are shown in Fig. 10. After excitation at 374 nm,  $\text{Tb}^{3+}$ -containing bioactive glass particles yielded violet (416 nm), blue (436 nm and 488 nm), green (544 nm), yellow (584 nm) and red (622 nm) fluorescence. The first group of emissions (violet and blue) at 416 and 436 nm are assigned to  ${}^5\text{D}_3 \rightarrow {}^7\text{F}_5$ ,  ${}^7\text{F}_4$  transitions [36, 37]. The second group of emissions at 488, 544, 584 and 622 nm are corresponding to  ${}^5\text{D}_4 \rightarrow {}^7\text{F}_6$ ,  ${}^7\text{F}_5$ ,  ${}^7\text{F}_4$  and  ${}^7\text{F}_3$  transitions, respectively [38]. Among them,  ${}^5\text{D}_4 \rightarrow {}^7\text{F}_5$  transition (544 nm) gave the most intense green emission. The photoluminescence spectra of  $\text{Tb}^{3+}$ -doped silicate-based 1393 glasses exhibited intense emission in green region and weak emission in blue region under 374 nm excitation. An increase in radiation emission was recorded as the  $\text{Tb}^{3+}$  concentration was ascended in the glass composition. Highest radiation intensity was observed for 5%Tb-containing 1393 glass particles. Similarly, terbium-containing bioactive glass nanofibers exhibited exactly the same emission spectrum upon excitation at 375 nm. However, their emission intensities were weaker almost fivefold compared to the PL intensity of sol–gel-

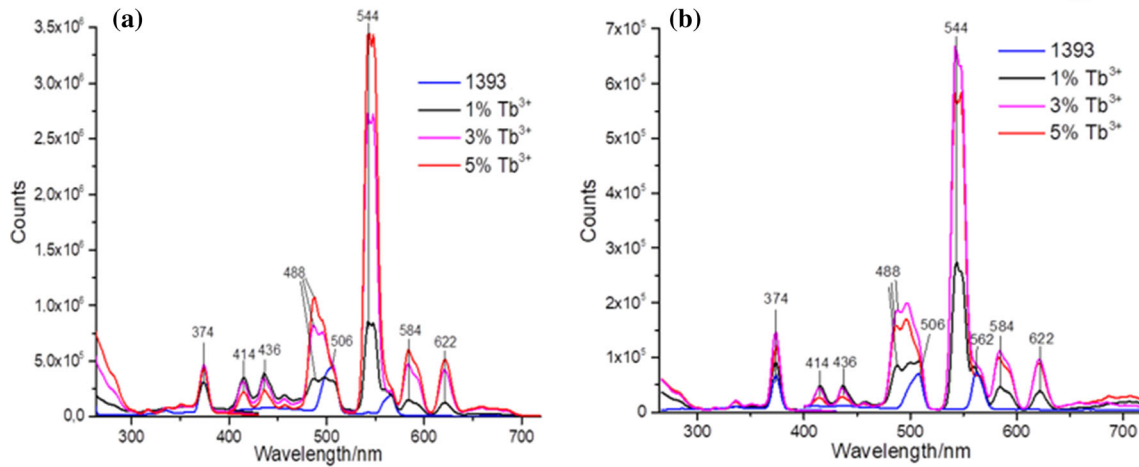


**Figure 10** Excitation and emission spectra of the  $Tb^{3+}$ -containing bioactive glass **a** particles, **b** nanofibers.

derived bioactive glass particles doped with  $Tb^{3+}$  at the same concentrations.

The PL emission spectra of the Er:Tb-1393 series bioactive glass particles and nanofibers in the wavelength range of 250–800 nm were given in Fig. 11. Accordingly, similar to the  $Er^{3+}$  or  $Tb^{3+}$ -containing bioactive glasses, upon excitation at 374 nm, the  $Er^{3+}:Tb^{3+}$  co-doped 1393 glass particles yielded violet (416 nm), blue (436 nm), green (506, 544 and 566 nm), yellow (584 nm) and red (622 nm) fluorescence and the green emission was the most intense among them. A similar PL spectrum was observed for the  $Er^{3+}:Tb^{3+}$ -1393 glass nanofibers, having weaker emission intensities compared to the co-doped glass particles, especially for the band at 544 nm. After the optimization of the dopant concentration, the gathered emission spectra of the dopant-free, 1%  $Er^{3+}$ , 5%  $Tb^{3+}$  and 3%  $Er^{3+}:Tb^{3+}$ -co-doped bioactive glasses

and electrospun fibers were shown in Fig. 12. As can be clearly observed from Fig. 12, the best results were obtained when  $Tb^{3+}$  was present at 5% in the glass samples.

### Florescence decay analysis

The fluorescence lifetime belongs to the excited state behavior of a fluorescent material. Decay kinetics of all of the bioactive glass samples in the form of particle and nanofiber were recorded in nanosecond, microsecond and millisecond time scales, respectively. The fluorescence lifetime data of the samples were acquired in solid state, on a solid sample holder. Each sample was irradiated with a 367.8 nm pulsed light source and a microsecond flash lamp, and the data acquisition was performed at emission

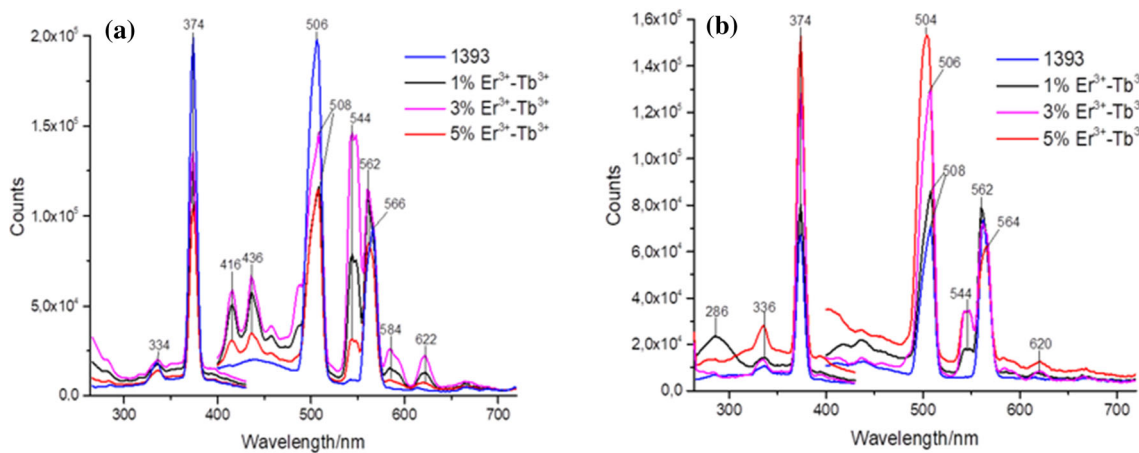


**Figure 11** Excitation and emission spectra of the  $Er^{3+}:Tb^{3+}$ -containing bioactive glass **a** particles, **b** nanofibers.

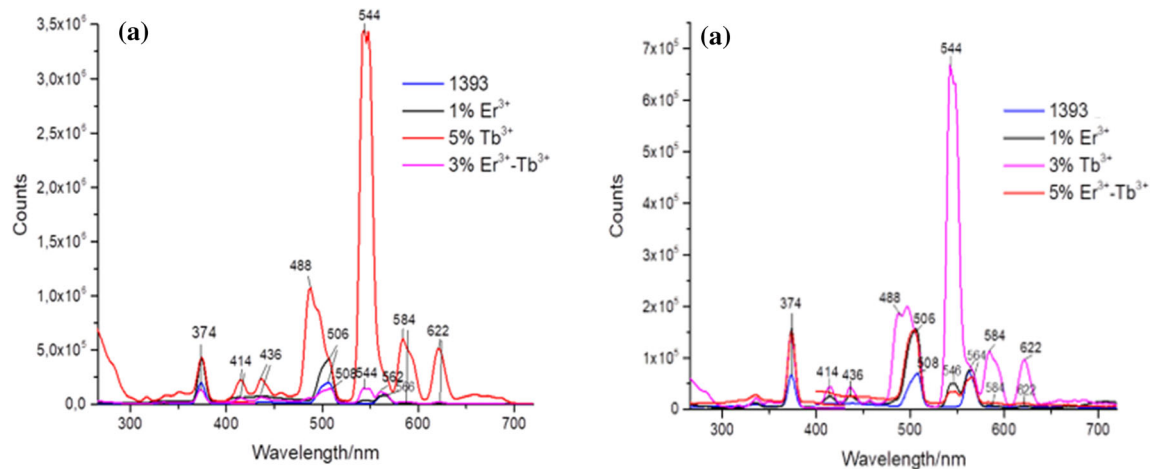


**Figure 12** Gathered excitation–emission spectra of the dopant-free,  $\text{Er}^{3+}$ ,  $\text{Tb}^{3+}$  and  $\text{Er}^{3+}:\text{Tb}^{3+}$ -co-doped bioactive glass **a** particles, **b** nanofibers.

maximum of each sample. In all cases, the samples exhibited multi-exponential decay.

The decays of the PL intensities were recorded on the basis of the exponential formula (Eq. 1). The fluorescence lifetime was determined the time after which the intensity is dropped to  $1/e$ , from the initial value.

$$I(t) = Ae^{(-t/\tau_1)} + Be^{(-t/\tau_2)} \quad (1)$$

The curves were fitted with bi-exponential equations (Eq. 1) where  $I(t)$  is the luminescence intensity as a function of time,  $A$  and  $B$  are constants and  $\tau$  is the decay time (see Fig. 13).

Tables 3 and 4 reveal bi-exponential decay data of the  $\text{Er}^{3+}$ ,  $\text{Tb}^{3+}$  and  $\text{Er}^{3+}:\text{Tb}^{3+}$  co-doped 1393 glass particles and electrospun fibers for the nanosecond, microsecond and millisecond time scales, respectively. The average decay times were calculated by taking the weighted average of multi-exponential decay times. The dopant-free 1393 glass particles exhibited bi-exponential decay when excited at 368 nm. In nanosecond time regime, the short and long lifetime components of the bare 1393 bioactive glass powders were measured to be 1.85 ns and 32.6 ns, respectively. Decay times of 1.99 (15%) and 11.1 (85%) microseconds were recorded for the bare glass particles.

When excited by 367.8 nm pulsed laser, in nanosecond timescale, the 1% $\text{Er}^{3+}$ -containing particles exhibited bi-exponential decays of 1.35 ns (55%) and 41.10 ns (45%) corresponding to average decay time of 19.17 ns. On the other hand, the

5% $\text{Tb}^{3+}$ -doped and 3% $\text{Er}^{3+}:\text{Tb}^{3+}$  co-doped particles exhibited 21.90 and 27.51 ns of average decay times, respectively (see Fig. 13a). Decay times were measured to be 9.85, 10.47 and 10.46  $\mu\text{s}$  for the  $\text{Er}^{3+}$ ,  $\text{Tb}^{3+}$  and  $\text{Er}^{3+}:\text{Tb}^{3+}$  co-doped particles, respectively, in the microsecond time regime (see Fig. 13b). In all cases, the decay curves exhibited bi-exponential behavior indicating the presence of two distinct decay channels. In millisecond timescale, 0.06, 2.97 and 2.11 ms of average decay times were recorded for the  $\text{Er}^{3+}$ ,  $\text{Tb}^{3+}$ , and the  $\text{Er}^{3+}:\text{Tb}^{3+}$  co-doped forms, respectively, which is in accordance with literature [39] (see Fig. 13c). Similar type of decay behavior was obtained for the bioactive glass nanofibers (see Fig. S1) Percentage distribution of the short and long lifetime components of the decays and further details including concentration dependency of the decay times and decay behavior of the bioactive glasses and the electrospun fibers are shown in Tables 3, 4 and Tables S1 and S2, respectively. The variations in the measured decay times arising from the morphological factors and non-crystalline structure of the bioactive glasses and fibers are an expected result.

The recorded nanosecond decay times can be assigned to photo-excitation of free excitations and their trapping at defect sites in the non-crystalline glassy matrix. The recorded microsecond scale lifetimes can be related to the presence of the deeply trapped holes. Herein, due to the presence of the free charge carriers and their efficient migration, and recombination in the amorphous structures, short and long luminescence decay time components in the nanosecond and microsecond time scale were

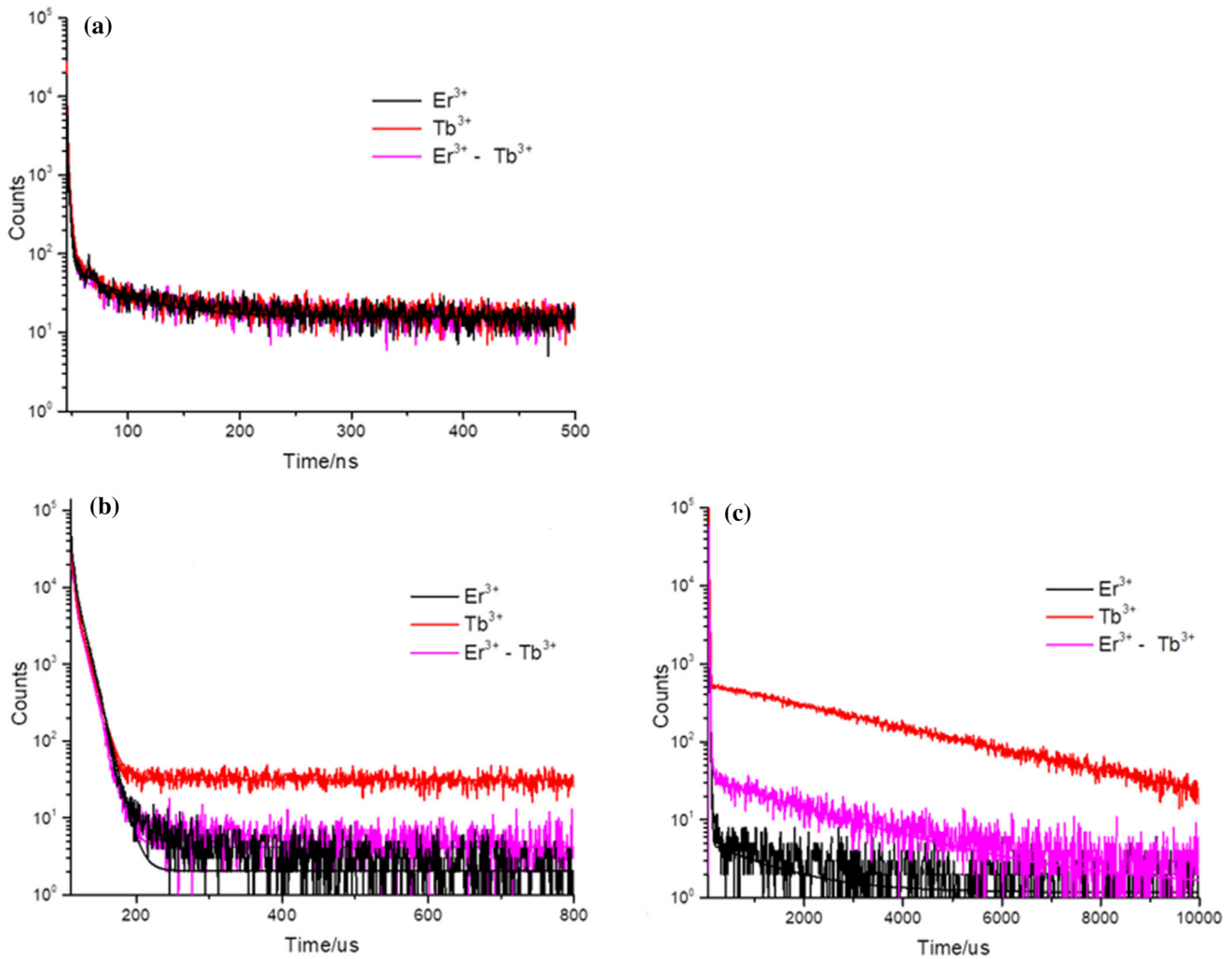


**Figure 13** Decay curves of the bioactive glass particles (based on the dopant concentration given in Fig. 12) in three different timescales: **a** nanosecond, **b** microsecond, **c** millisecond time scale.

recorded. On the other hand, the recorded millisecond decays can be assigned to the existence previously explained transitions of  $\text{Er}^{3+}$  and  $\text{Tb}^{3+}$  ions in the matrix. In all cases, co-existence of the  $\text{Er}^{3+}$  and  $\text{Tb}^{3+}$  ions within the same matrix did not make a significant effect neither in decay times nor in fluorescent intensities. Compared to the glass particles, in nanofibers, generally the slow component of the decay time was more dominant. The fast component has been reported to be related to excitation spontaneous recombination, while the slower component could be attributed to trapping/detrapping mechanisms [40].

The luminescence decay time imaging has been evaluated as an alternative method in bioimaging studies previously [40, 41]. The presence of different fluorescence excited state lifetimes is generally

required to solve the difficulties observed for the recognition of different fractions of the same fluorophore in different states in the molecular structure. This may require to use of the luminescent materials having multi-exponential decay characteristics. In the study, all of the glass samples exhibited bi-exponential decay behavior which can be concluded as an advantage from this point of view.

Finding of the current study also indicated that the luminescence intensity and the decay times of the  $\text{Er}^{3+}$  and  $\text{Tb}^{3+}$  -doped bioactive glass samples were dependent on the sample morphology. Although emission intensities of the bioactive glass samples in the form particles were stronger compared to the samples in the form of nanofibers, in terms of decay time analysis nanofibers showed better performance exhibiting longer average decay times. Previously, it

**Table 3** Decay time measurement results of the studied bioactive glass particles

Sample (particle)	$\tau_0$	Decay time (ns)	Std. Dev	Rel. (%)	$\tau_{avr}$ (ns)	Decay time ( $\mu$ s)	Std. Dev	Rel. (%)	$\tau_{avr}$ ( $\mu$ s)
1%Er <sup>3+</sup> doped	$\tau_1$	1.35	0.0313	55.19	19.17	1.94	0.0741	12.73	9.85
	$\tau_2$	41.10	1.7255	44.81		10.67	0.0417	87.27	
5%Tb <sup>3+</sup> doped	$\tau_1$	2.95	0.1522	41.52	21.90	1.15	0.1984	2.98	10.47
	$\tau_2$	35.36	2.5091	58.48		10.76	0.0498	97.02	
3%Er <sup>3+</sup> : Tb <sup>3+</sup> doped	$\tau_1$	3.42	0.3789	30.65	27.51	1.39	0.1805	3.84	10.46
	$\tau_2$	38.16	3.9903	69.35		10.79	0.0420	96.16	
Sample (particle)	$\tau_0$	Decay time (ms)			Std. Dev		Rel. (%)		$\tau_{avr}$ (ms)
1%Er <sup>3+</sup> doped	$\tau_1$	11.23			0.1314		96.32		0.06
	$\tau_2$	1250.40			169.4665		3.68		
5%Tb <sup>3+</sup> doped	$\tau_1$	6.94			0.3703		2.63		2.97
	$\tau_2$	3051.39			24.9721		97.37		
3%Er <sup>3+</sup> : Tb <sup>3+</sup> doped	$\tau_1$	21.26			4.2777		2.98		2.11
	$\tau_2$	2176.19			67.2413		97.02		

**Table 4** Lifetime measurement results of the studied bioactive electrospun nanofibers

Sample (nanofiber)	$\tau_0$	Decay time (ns)	Std. Dev	Rel. (%)	$\tau_{avr}$ (ns)	Decay time ( $\mu$ s)	Std. Dev	Rel. (%)	$\tau_{avr}$ ( $\mu$ s)
1%Er <sup>3+</sup> doped	$\tau_1$	2.29	0.0899	44.47	25.18	2.76	0.080	24.29	9.49
	$\tau_2$	43.50	2.5899	55.53		11.65	0.0746	75.71	
3%Tb <sup>3+</sup> doped	$\tau_1$	2.29	0.2528	20.32	29.48	1.80	0.1758	8.46	10.66
	$\tau_2$	36.42	2.3188	79.68		11.02	0.0802	91.54	
5%Er <sup>3+</sup> : Tb <sup>3+</sup> doped	$\tau_1$	3.37	0.4404	28.60	41.26	3.24	0.0913	30.10	11.19
	$\tau_2$	56.44	8.5892	71.40		15.27	0.1390	69.90	
Sample (nanofiber)	$\tau_0$	Decay time (ms)			Std. Dev		Rel. (%)		$\tau_{avr}$ (ms)
1%Er <sup>3+</sup> doped	$\tau_1$	11.08			0.0905		92.17		0.16
	$\tau_2$	1947.03			119.7026		7.83		
3%Tb <sup>3+</sup> doped	$\tau_1$	9.93			0.4002		7.83		2.91
	$\tau_2$	3151.92			61.5011		92.17		
5%Er <sup>3+</sup> : Tb <sup>3+</sup> doped	$\tau_1$	11.81			0.4994		49.87		0.15
	$\tau_2$	290.95			9.4981		50.13		

has been reported that the photoluminescence lifetime excited by electron or laser radiation strongly varies as a function of the size and morphology of the particles [42]. Silver et al. [43] investigated the influence of particle morphology as well as the crystallite size on the upconversion luminescent properties of Er<sup>3+</sup> and Yb<sup>3+</sup> co-doped yttrium oxide phosphors. Results revealed that the most intense yellow-green upconversion emission occurred when the larger size particles utilized and the cross-relaxation processes between Er<sup>3+</sup> ions are responsible for the efficient upconversion in these larger particles. Kim and Kang

[44] studied on the influence of particle size on photoluminescence emission intensity for ZnO in the form of powders and nano-rods. The results obtained from powder samples were similar to those from nano-rod samples and green emission intensity greatly increased by the increase in particle size. Similarly, Lisitsyn et al. [42] reported that for the ZnWO<sub>4</sub>, the most extended decay time was recorded for samples with coarser particles. On the other hand, in samples with nanoparticles the characteristic decay times ranged from 5 to 7  $\mu$ s, that is, much

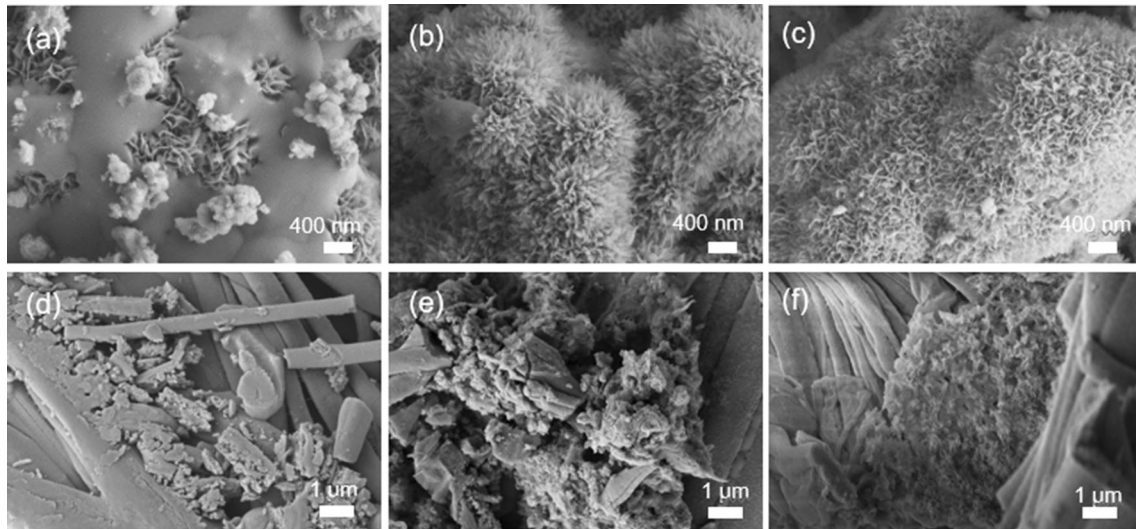


**Figure 14** SEM micrographs of the bioactive glass samples treated in SBF for 30 days. **a** 1393 particle, **b** 5%Er-1393 particle, **c** 5%Tb-1393, **d** 1393 fiber, **e** 5%Er-1393 fiber, **f** 5%Tb-1393 fiber.

smaller compared to the crushed single crystal particles ( $\tau = 15\text{--}20 \mu\text{s}$ ).

In the current study, difference observed in photoluminescence properties of 1393 based bioactive glass samples in the form of particles and fibers can also be attributed to the differences in their size. Bioactive glass fiber mats tend to form agglomerated short fibers after chopping. Compared to the bioactive glass particles with an average particle size of  $\sim 1.5\text{--}3.5 \mu\text{m}$ , rod-like short fiber samples have smaller diameter and larger rod length. It has been reported that the electron structure of particles is strongly sensitive to the local field that is dependent on the particle size [45]. The change in particle size causes to change in the band gap of the glass particle [42]. The luminescence from the bulk of a particle is evaluated by the periodic potential; on the other hand, the surface related to photon generation is affected by the surface energy. When the size of the near-surface region is close to the size of the bulk, the photons from both of them affect the luminescence features. However, if the particulate size gets smaller compared to the bulk exciton radius, quantum confinement effects are observed.

Therefore, in the current study, the difference observed in PL intensities may be due to the difference in the energy structure of the samples as well as the defects based on the size of the nanofibers. Additionally, fluorescence lifetime may be dependent on some factors such as polarity and the existence of the fluorescence quenchers as well as the intrinsic

parameters which are influenced by fluorophore structure [46]. In addition since PL luminescence decays with time due to fluorescence emission and non-radiative processes [47], later may be a factor for the shorter decay times recorded for the glass particles.

### In vitro bioactivity

Figure 14 depicts the SEM micrographs of the SBF-treated bioactive glass samples in the form of particles and nanofibers. Accordingly, there is a second-phase material formation on the surface of the all materials, which is presumably a crystalline hydroxyapatite. The plate-like morphology of the deposited material is well agreed with the typical morphology of HA [48, 49]. Results revealed that the  $\text{Er}^{3+}$  and  $\text{Tb}^{3+}$  substitution even at highest concentration (5 wt%) did not cause any deleterious influence on the HA formation ability of the bioactive glass samples. Similarly, at other dopant concentrations, a decrease in bioactivity of the glass samples was not observed compared to the bare 1393 glass. Based on the SEM micrographs, it was also concluded that HA formation amount on the surface of the sol-gel derived glass powders was higher compared to electrospun nanofibers. The in vitro bioactivity of the luminescent bioactive glasses prepared in the study demonstrates their potential to be used in bone tissue engineering applications.

## Conclusions

Erbium- and terbium-doped 1393 bioactive glass particles ( $d_{50} = \sim 1.5\text{--}3.5 \mu\text{m}$ ) and nanofibers (diameter: 280–660 nm) were synthesized using sol–gel and electrospinning methods, respectively. Luminescent properties of the  $\text{Er}^{3+}$  and  $\text{Tb}^{3+}$ -containing glass samples have been investigated in comparison with bare 1393 bioactive glass by steady-state and time-resolved spectroscopy. Both undoped and erbium-doped 1393 bioactive glasses exhibited green luminescence upon excitation at 374 nm. Terbium-activated samples also demonstrated emissions centered at 488, 544, 584 and 622 nm. All of the glass formulations prepared in the study exhibited bi-exponential decay when excited at 374 nm. The monitored two exponential decay times in the doped glass samples may be due to the structural characteristics of the host, the existence of different emission centers for  $\text{Er}^{3+}$  and  $\text{Tb}^{3+}$ , as well as their transitions in the glass network. Results showed that the optimum concentration of the activator ions for the 1393 bioactive glass particles was 1 wt%  $\text{Er}^{3+}$  and 5 wt%  $\text{Tb}^{3+}$  in terms of luminescent intensity. Presence of the  $\text{Er}^{3+}$  and  $\text{Tb}^{3+}$  ions in the glass network induced an enrichment in the decay times and extended decay times was obtained both in microsecond and nanosecond time regime measurements as the dopant concentration was increased. For the 5% $\text{Er}^{3+}$ : $\text{Tb}^{3+}$  co-doped bioactive glass nanofibers highest decay times were recorded as 41.26 ns and 11.19  $\mu\text{s}$  in the nanosecond and microsecond time regimes, respectively. Results also revealed that bioactive glass morphology significantly affects the luminescence emission intensity as well as the decay kinetics. Sol-gel derived bioactive glass particles exhibited stronger emission intensity whereas electrospun nanofibers showed extended decay times.  $\text{Er}^{3+}$  and  $\text{Tb}^{3+}$  doping did not cause any adverse influence on the in vitro bioactivity of the prepared glass compositions. Investigating the time-dependent hydroxyapatite forming ability and in vitro biocompatibility of the prepared luminescent bioactive glasses for bone tissue engineering purposes will be the goal of the future study.

## Acknowledgements

The financial support of The Scientific and Technological Research Council of Turkey (TUBITAK), Grant No: 119M934, is gratefully acknowledged. Photoluminescence characterizations were performed at Dokuz Eylul University, Center for Production and Applications of Electronic Materials (EMUM). The SEM and XRD analysis were performed at Manisa Celal Bayar University—Applied Science and Research Center (DEFAM).

## Declarations

**Conflict of interest** The authors declare that they have no conflict of interest.

**Supplementary Information:** The online version contains supplementary material available at <http://doi.org/10.1007/s10853-021-06203-7>.

## References

- [1] Lu H, Chen F, Xi P, Chen B, Huang L, Cheng J, Shao C, Wang J, Bai D, Zeng Z (2011) Biocompatible fluorescent hydroxyapatite: synthesis and live cell imaging applications. *J Phys Chem C* 115:18538–18544. <https://doi.org/10.1021/jp206843w>
- [2] Neacsu IA, Stoica AE, Vasile BS, Andronescu E (2019) Luminescent hydroxyapatite doped with rare earth elements for biomedical applications. *Nanomaterials* 9(2):239. <https://doi.org/10.3390/nano9020239>
- [3] Grabmaier BC (1994) Luminescent materials for medical application. *J Lumin* 60–61:967–970. <https://doi.org/10.3390/nano9020239>
- [4] Gerhard L-C, Boccaccini AR (2010) Bioactive glass and glass-ceramic scaffolds for bone tissue engineering. *Materials* 3:3867–3910. <https://doi.org/10.3390/ma3073867>
- [5] Hench LL, Splinter RJ, Allen WC, Greenlee TK Jr (1971) Bonding mechanisms at the interface of ceramic prosthetic materials. *J Biomed Mater Res* 2:117–141. <https://doi.org/10.1002/jbm.820050611>
- [6] Hench LL, Wilson J (1984) Surface active biomaterials. *Science* 226:630–636. <https://doi.org/10.1126/science.6093253>
- [7] Rahaman MN, Day DE, Bal BS, Fu Q, Jung SB, Bonewald LF, Tomsia AP (2011) Bioactive glass in tissue engineering. *Acta Biomater* 7(6):2355–2373. <https://doi.org/10.1016/j.actbio.2011.03.016>



- [8] Brink M, Turunen T, Happonen R, Yli-Urpo A (1997) Compositional dependence of bioactivity of glasses in the system  $\text{Na}_2\text{O-K}_2\text{O-MgO-CaO-B}_2\text{O}_3\text{-P}_2\text{O}_5\text{-SiO}_2$ . *J Mater Sci Mater Med* 37:114–121. [https://doi.org/10.1002/\(sici\)1097-4636\(199710\)37:1<114::aid-jbm14>3.0.co;2-g](https://doi.org/10.1002/(sici)1097-4636(199710)37:1<114::aid-jbm14>3.0.co;2-g)
- [9] Fan Y, Yang P, Huang S, Jiang J, Lian H, Lin J (2009) Luminescent and mesoporous europium-doped bioactive glasses (MBG) as a drug carrier. *Phys Chem C* 113(18):7826–7830. <https://doi.org/10.1021/jp900515x>
- [10] Li G, Liang G, Zhao S, Ma K, Feng W, Zhou D, Liu X (2014) Synthesis and characterization of porous luminescent glass ceramic scaffolds containing europium for bone tissue engineering. *Adv Appl Ceram*. 114(3):164–174. <https://doi.org/10.1179/1743676114Y.000000021>
- [11] Saarinen M, Nommeots-Nomm A, Hokka M, Laurila J, Norrbod I, Lastusaari M, Massera J, Petit L (2018) Persistent luminescent particles containing bioactive glasses: Prospect toward tracking in-vivo implant mineralization using biophotonic ceramics. *J Eur Ceram Soc* 38:287–295. <https://doi.org/10.1016/j.jeurceramsoc.2017.08.024>
- [12] Ganjali MR, Gupta KV, Faridbod GF, Norouzi P (2016) Lanthanides series determination by various analytical methods. Chapter 2, Applications of the lanthanide series in human life. pp 37–58. <https://doi.org/10.1016/B978-0-12-804704-0.00002-5>
- [13] Patnaik P (2002) Handbook of inorganic chemicals. McGraw-Hill
- [14] Alshemary AZ, Akram M, Goh Y-F, Abdul Kadir MR, Abdolahi A, Hussain R (2015) Structural characterization, optical properties and in vitro bioactivity of mesoporous erbium-doped hydroxyapatite. *J Alloys Compd* 645:478–486. <https://doi.org/10.1016/j.jallcom.2015.05.064>
- [15] Pham V-H, Van HN, Tam PD, Ha HNT (2016) A novel 1540 nm light emission from erbium doped hydroxyapatite/-tricalcium phosphate through co-precipitation method. *Mater Lett* 167:145–147. <https://doi.org/10.1016/j.matlet.2016.01.002>
- [16] Mondal S, Nguyen VT, Park S, Choi J, Tran LH, Yi M, Shin JH, Lee C-Y, Oh J (2020) Bioactive, luminescent erbium-doped hydroxyapatite nanocrystals for biomedical applications. *Ceram Int* 46(10):16020–16031. <https://doi.org/10.1016/j.ceramint.2020.03.152>
- [17] Li Q, Xing M, Chen Z, Wang X, Zhao C, Qiu J, Jianding Yu, Chang J (2016)  $\text{Er}^{3+}/\text{Yb}^{3+}$  co-doped bioactive glasses with up-conversion luminescence prepared by containerless processing. *Ceram Int* 42(11):13168–13175. <https://doi.org/10.1016/j.ceramint.2016.05.108>
- [18] Hammond CR (2000) The elements in handbook of chemistry and physics. CRC Press
- [19] Wang X, Zhang Y, Lin C, Zhong W (2017) Sol-gel derived terbium-containing mesoporous bioactive glasses nanospheres: in vitro hydroxyapatite formation and drug delivery. *Colloids Surf B* 160:406–415. <https://doi.org/10.1016/j.colsurfb.2017.09.051>
- [20] Qiao Y, Li Y-X, Yin H-R, Liu P, Li S-Y, Zhang P (2015) Preparation and luminescent properties of terbium-doped hydroxyapatite. *Chin J Lumin* 36(1):63–68. <https://doi.org/10.3788/fjxb20153601.0063>
- [21] Deliormanlı AM, Yıldırım M (2016) Sol-gel synthesis of 13–93 bioactive glass powders containing therapeutic agents. *J Aust Ceram Soc* 52(2):9–19
- [22] Deliormanlı AM (2015) Preparation in vitro mineralization and osteoblast cell response of 13–93 bioactive glass nanofibers for biomedical applications. *Mater Sci Eng C Mater Biol Appl* 53:262–271. <https://doi.org/10.1016/j.msec.2015.04.037>
- [23] Kokubo T, Kushitani H, Sakka S, Kitsugi T, Yamamuro T (1990) Solutions able to reproduce in vivo surface-structure change in bioactive glass-ceramic A-W. *J Biomed Mater Res* 24:721–734. <https://doi.org/10.1002/jbm.820240607>
- [24] Silva AMB, Queiroz CM, Agathopoulos S, Correia RN, Fernandes MHV, Oliveira JM (2011) Structure of  $\text{SiO}_2\text{-MgO-Na}_2\text{O}$  glasses by FTIR, Raman and  $^{29}\text{Si}$  MAS NMR. *J Mol Struct* 986:16–21. <https://doi.org/10.1016/j.molstruc.2010.11.023>
- [25] Wong J, Angell CA (1976) Glass structure by spectroscopy. Marcel Dekker, New York
- [26] Nariyal RK, Kothari P, Bisht B (2014) FTIR measurements of  $\text{SiO}_2$  glass prepared by sol-gel technique. *Chem Sci Trans* 3(3):1064–1066. <https://doi.org/10.7598/cst2014.816>
- [27] Nakamoto K (1997) Infrared and raman spectra of inorganic and coordination compounds: part A—theory and applications in inorganic chemistry, 5th edn. Wiley, New York
- [28] Carter CB, Norton MG (2013) Ceramic materials: science and engineering. Complex crystal and glass structures (Chap. 7). Springer, pp 103–122. [https://doi.org/10.1007/978-1-4614-3523-5\\_7](https://doi.org/10.1007/978-1-4614-3523-5_7)
- [29] Xu GQ, Zheng ZX, Tang WM, Wu YC (2007) Multi-peak behavior of photoluminescence of silica particles heat-treated in hydrogen at elevated temperature. *J Lumin* 126:43–47. <https://doi.org/10.1016/j.jlumin.2006.05.001>
- [30] Ehrhart D, Ebeling P (2003) Radiation defects in borosilicate glasses. *Glass Technol* 44(2):46–49
- [31] de Dood MJA, Slooff LH, Polman A, Moroz A, van Blaaderen A (2001) Modified spontaneous emission in erbium-doped  $\text{SiO}_2$  spherical colloids. *Appl Phys Lett* 79(22):3585–3587. <https://doi.org/10.1063/1.1419033>
- [32] Said Mahraz ZA, Sahar MR, Ghoshal SK, Reza Dousti M (2013) Concentration dependent luminescence quenching of

- Er<sup>3+</sup>-doped zinc boro-tellurite glass. *J Lumin* 144:139–145. <https://doi.org/10.1016/j.jlumin.2013.06.050>
- [33] Lo Savio R, Miritello M, Cardile P, Priolo F (2009) Concentration dependence of the Er<sup>3+</sup> visible and infrared luminescence in Y<sub>2-x</sub>Er<sub>x</sub>O<sub>3</sub> thin films on Si. *J Appl Phys* 106:043512. <https://doi.org/10.1063/1.3195077>
- [34] Ehrst D (2011) Photoactive glasses and glass ceramics. *IOP Conf Ser Mater Sci Eng* 21:012001
- [35] Wojdak M, Jayatilleka H, Shah M, Kenyon AJ, Gourbilleau F, Rizk R (2013) Modification of erbium photoluminescence decay rate due to ITO layers on thin films of SiO<sub>2</sub>: Er doped with Si-nanoclusters. *J Lumin* 136:407–410. <https://doi.org/10.1016/j.jlumin.2012.11.042>
- [36] Sun XY, Huang SM, Gu M, Gao QC, Gong XS, Ye ZP (2010) Enhanced Tb<sup>3+</sup> luminescence by non-radiative energy transfer from Gd<sup>3+</sup> in silicate glass. *Phys B* 405:569–572. <https://doi.org/10.1016/j.physb.2009.09.067>
- [37] Sun XY, Yu XG, Wang WF, Li YN, Zhang ZJ, Zhao JT (2013) Luminescent properties of Tb<sup>3+</sup>-activated B<sub>2</sub>O<sub>3</sub>-GeO<sub>2</sub>-Gd<sub>2</sub>O<sub>3</sub> scintillating glasses. *J Non-Cryst Solids* 379:127–130. <https://doi.org/10.1016/j.jnoncrystol.2013.08.002>
- [38] Sun XY, Jiang DG, Wang WF, Cao CY, Li YN, Zhen GT, Wang H, Yang XX, Chen HH, Zhang ZJ, Zhao JT (2013) Luminescence properties of B<sub>2</sub>O<sub>3</sub>-GeO<sub>2</sub>-Gd<sub>2</sub>O<sub>3</sub> scintillating glass doped with rare-earth and transition-metal ions. *Nucl Inst Methods Phys Res A* 716:90–95. <https://doi.org/10.1016/j.nima.2013.03.036>
- [39] Kik PG, Polman A (2001) Exciton-erbium energy transfer in Si nanocrystal-doped SiO<sub>2</sub>. *Mater Sci Eng B* 81(1–3):3–8. [https://doi.org/10.1016/S0921-5107\(00\)00667-X](https://doi.org/10.1016/S0921-5107(00)00667-X)
- [40] Bei J, Qian G, Liang X, Yuan S, Yang Y, Chen G (2007) Optical properties of Ce<sup>3+</sup>-doped oxide glasses and correlations with optical basicity. *Mater Res Bull* 42:1195–1200. <https://doi.org/10.1016/j.materresbull.2006.10.020>
- [41] Yao Y, Liu L, Zhang Y, Chen D, Fang Y, Zhao G (2016) Optical properties of Ce<sup>3+</sup> doped fluorophosphates scintillation glasses. *Opt Mater* 51:94–97. <https://doi.org/10.1016/j.optmat.2015.11.026>
- [42] Lisitsyn VM, Valiev DT, Tupitsyna IA, Polisadova EF, Oleshko VI, Lisitsyna LA, Andryuschenko LA, Yakubovskaya AG, Vovk OM (2014) Effect of particle size and morphology on the properties of luminescence in ZnWO<sub>4</sub>. *J Lumin* 153:130–135. <https://doi.org/10.1016/j.jlumin.2014.03.024>
- [43] Silver J, Martinez-Rubio MI, Ireland TG, Fern GR, Withnall R (2001) The effect of particle morphology and crystallite size on the upconversion luminescence properties of erbium and ytterbium co-doped yttrium oxide phosphors. *J Phys Chem B* 105(5):948–953. <https://doi.org/10.1021/jp002778c>
- [44] Kim Y, Kang S (2011) Effect of particle size on photoluminescence emission intensity in ZnO. *Acta Mater* 59(8):3024–3031. <https://doi.org/10.1016/j.actamat.2011.01.042>
- [45] Kislyuk V, Strilchuk G, Lozovski V, Osipyonok M, Lytvyn P (2004) Influence of particle size on luminescence spectra. *Progr Colloid Polym Sci* 125:24–26. [https://doi.org/10.1007/978-3-540-45119-8\\_4](https://doi.org/10.1007/978-3-540-45119-8_4)
- [46] Berezin MY, Achilefu S (2010) Fluorescence lifetime measurements and biological imaging. *Chem Rev* 110(5):2641–2684. <https://doi.org/10.1021/cr900343z>
- [47] Jain A, Blum C, Subramaniam V (2009) Advances in biomedical engineering, Chapter 4, Fluorescence lifetime spectroscopy and imaging of visible fluorescent proteins. pp 147–176. <https://doi.org/10.1016/B978-0-444-53075-2.0004-6>
- [48] Larrañaga A, Ramos D, Amestoy H, Zuza E, Sarasua J-R (2015) Coating of bioactive glass particles with mussel-inspired polydopamine as a strategy to improve the thermal stability of poly(L-lactide)/bioactive glass composites. *RSC Adv* 5:65618–65626. <https://doi.org/10.1039/C5RA09495J>
- [49] Miola M, Verné E, Cirraldo FE, Cordero-Arias L, Boccaccini AR (2015) Electrophoretic deposition of chitosan/45S5 bioactive glass composite coatings doped with Zn and Sr. *Front Bioeng Biotechnol* 3:159. <https://doi.org/10.3389/fbioe.2015.00159>

**Publisher's Note** Springer Nature remains neutral with regard to jurisdictional claims in published maps and institutional affiliations.